Available online at www.sciencedirect.com

jmr&t
Journal of Materials Research and Technology

journal homepage: www.elsevier.com/locate/jmrt

Original Article

Molecular interfacial properties and engineering performance of conductive fillers in cementitious composites

Junbo Sun [a,b], *Yufei Wang* [a], *Kefei Li* [c], *Xupei Yao* [d,*], *Binrong Zhu* [e], *Jiaqing Wang* [f], *Qianqian Dong* [g], *Xiangyu Wang* [a,**]

[a] School of Design and Built Environment, Curtin University, WA 6102, Australia
[b] Institute for Smart City of Chongqing University in Liyang, Chongqing University, Jiangsu, 213300, PR China
[c] School of Civil and Environmental Engineering, University of New South Wales, Sydney, NSW 2052, Australia
[d] Department of Civil Engineering, Monash University, Clayton, Victoria, 3800, Australia
[e] School of Civil Engineering, Southeast University, Nanjing 211189, PR China
[f] College of Civil Engineering, Nanjing Forestry University, Jiangsu 210037, PR China
[g] College of Aerospace and Civil Engineering, Harbin Engineering University, PR China

ARTICLE INFO

Article history:
Received 8 March 2022
Accepted 9 May 2022
Available online 16 May 2022

Keywords:
Electrically conductive cementitious composites
Molecular dynamic simulation
Waste slag
Compressive strength
Flexural strength
Electrical resistivity

ABSTRACT

Conductive fillers, such as graphite particles (GP), steel slags (SS), and ground granulated blast furnace slag (GGBS) have been widely utilized in designing electrically conductive cementitious composites (ECCC) for various applications, including traffic detection, structural health monitoring (SHM), and pavement deicing. Owing to the complex working field, a comprehensive understanding of the role that the conductive fillers played in ECCC is essential for designing high-performance ECCC. In the present study, mechanical and conductivity experiments were conducted to explore the influences of these fillers on ECCC performances in strengths and electrical resistance. In addition, the reactive molecular dynamic (MD) simulation was firstly performed to quantify the interfacial properties of GP, SS, and GGBS in ECCC at the molecular level. Simulation results indicated that the chemical components of these conductive fillers dominate the atomic interfacial properties. Mineral components in SS or GGBS, especially Al_2O_3 and SiO_2, led to a stronger interfacial bonding with cement in comparison to graphite in GP. At last, a hybrid mixing design of GP and SS was proposed in this study, balancing the mechanical and conductive performance of ECCC.

* Corresponding author.
** Corresponding author.
E-mail addresses: xupei.yao@monash.edu (X. Yao), Xiangyu.Wang@curtin.edu.au (X. Wang).
https://doi.org/10.1016/j.jmrt.2022.05.061

1. Introduction

To halt the increasingly serious global warming, reducing CO_2 emissions and achieving carbon neutrality has become a global consensus in many countries according to Paris Agreement [1,2]. However, owing to the intrinsic manufacturing process of cement, where a large amount of fossil fuels is required, achieving carbon neutrality is challenging in the cement industry [3,4]. Production of 1-tonne cement clinkers releases 0.86 tons of CO_2 [5,6]. Consequently, given that Portland cement is the most consumed manufactured material, the fabrication of cement accounts for around 5% of global CO_2 emissions [7–9]. Therefore, substitute materials of cement clinkers in concrete have been rapidly developed in recent years [10–12].

To suit the various and complex working fields, cementitious composites with these substitute materials should not only own excellent mechanical properties but also possess functionality for different applications [13–15]. For example, fillers with specific electrical conductivity, such as steel slags (SS) [16], ground granulated blast-furnace slag (GGBS), and graphite powder (GP) [17], were employed as partial replacements for cement clinkers to make electrically conductive cementitious composites (ECCC), which has a wide application in traffic detection, structural health monitoring and pavement deicing [18–20]. The mechanism to achieve these benefits derives from the piezoresistivity effect, laying foundations for measurements of the altered electrical resistivity as well as strain or stress changes in structures [21]. Among those fillers, the addition of GP significantly improved the electrical conductivity of ECCC by reducing the resistance [22,23]. However, since GP is of weak interlayer shear strength and has a weak interaction with cement, incorporation of GP negates the mechanical properties of ECCC [24–26]. For instance, Sun, Lin [27] reported that ever explored that a 4% increase in GP content led to the 23–43% drop in uniaxial compressive strength (UCS) values compared to the control sample when fixing other additives. Thereby, some metal waste slags, such as SS and GGBS, are introduced to balance the conductive and mechanical performance of ECCC according to their metal oxides (especially iron oxides) and pozzolanic properties [28].

SS, as well as GGBS, are produced from the steel industry and usually discarded in landfills, resulting in numerous environmental problems [29,30]. Therefore, recycling and reusing them in producing cementitious composite are also urgent and feasible from the aspect of sustainability [8,31]. The replacement of cement with SS has been verified to remarkably improve the compressive strength, and simultaneously reduce the electrical resistance of ECCC [32]. The improvement in electrical conductivity of ECCC is mainly attributed to the enriched ferrite content of SS or GGBS, showing considerable conductive properties [33,34]. For instance, ferrites of SS contain FeO and Fe_3O_4, which have a low electrical resistivity of around 5×10^{-2} and 4×10^{-3} Ω cm, respectively, satisfying the demand for ECCC production [35]. As for mechanical performance, the mineral composition of SS or GGBS, such as Fe_2O_3, Al_2O_3, and SiO_2, enabled a strong interaction with cement, which enhanced the interfacial bonding between fillers and cementitious matrix [36,37]. However, despite the intensive research efforts, the role of these conductive fillers at the molecular scale and their implication for the engineering performance of ECCC are lack quantification, which greatly limited their application for high-performance ECCC.

In the present study, the engineering performance of ECCC with conductive fillers comprising GP, SS, and GGBS, was initially investigated by testing the compressive strength, flexural strength, and electrical conductivity. A framework was then proposed connecting the atomic interfacial properties with the engineering performance of ECCC to identify the role of these fillers. Reactive molecular dynamic (MD) simulation was therefore employed to quantify the interfacial properties between the conductive fillers and cement at the molecular level by conducting a shear test and identifying the corresponding distribution of shear stress. A scanning electron microscopy (SEM) was adopted to observe the microstructure of the ECCC around the fillers' vicinity. This study revealed that the chemical components of conductive fillers played an important role in their interfacial properties with cement, which consequently affected the mechanical performance of ECCC significantly. On the other hand, the electrical conductivity of ECCC was mainly dominated by the connectivity of the network formed by these conductive fillers. The findings in this study provided a deeper understanding of the role of the conductive fillers in improving the engineering performance of ECCC, which paved a way for the design of high-performance ECCC balancing the electrical conductivity and mechanical properties.

2. Methodology

2.1. Experimental methodology

2.1.1. Materials

The GP was supplied by GRF Ltd., Jiangsu, China, GGBS was supplied by Yuanheng Ltd., Henan, China, and SS was supplied by Hengyuan Ltd., Henan, China. These conductive fillers (GP, GGBS, and SS) were commercially available and their chemical compositions were shown in Table 1.

Silica sand and gravels of different sizes are utilized as fine and coarse aggregates respectively, as indicated in Table 2. The ordinary Portland cement with 42.5 MPa 28-day compressive strength (P.O. 42.5 R) conforming to the requirements of Australia Standard AS 3972 [38] was adopted as a cement binder in the prepared ECCC. A polycarboxylate superplasticizer (SP) is introduced to decrease the cement sensitivity and segregation stress.

Table 1 – Chemical compositions of conductive fillers.

	Fe2O3	Al2O3	SiO2	CaO	Carbon	Ash	Others
SS	21.30%	5.70%	14.60%	31.50%	–	–	26.90%
GGBS	1.80%	15.60%	31.00%	37.10%	–	–	14.50%
GP	–	–	–	–	98.50%	0.90%	0.60%

Table 2 – Physical and chemical characteristics of coarse aggregate and fine aggregate.

Coarse aggregate (CA)		Fine aggregate (FA)	
Sieve size	passing	Sieve size	
10 mm	100%	850 μm	0%
9 mm	87%	600 μm	0.30%
5 mm	20%	425 μm	11.90%
4.75 mm	7%	300 μm	40.80%
2.35 mm	4%	212 μm	31.60%
1.18 mm	3%	150 μm	12.60%
600 μm	2%	106 μm	2.30%
300 μm	2%		
150 μm	2%	Apparent particle density	2.76 t/m^3
75 μm	2%	Particle density dry	2.65 t/m^3
		Particle density	2.69 t/m^3
Moisture content	0.5%	Water absorption	1.40%
Flakiness index	24%	Moisture content	2.50%

2.1.2. *Specimen preparation*

GP, as the major additive, needs to be purified before sample preparations in this study. The explanation is impurities adhering to its surface cause mechanical strength reduction [39]. Original GP was firstly treated with acetone solution lasting for 60 min for activation and purification. After this, the soaked GP was heated through an oven by controlling the temperature at 60 °C for a few hours. Due to the fine and lightweight nature, GP was prone to accumulate and therefore destroy the mixture consistency in producing its solutions. To solve this, 10% dispersant and 5% coupling agent in proportion to GP weight were introduced to produce uniform GP solutions. Later, a 10 min ultra-sonication was required to check the performances of chemical additives. It is noted that the suspension solution was required to maintain room temperature (RT).

When the GP solution was finished, dry components including aggregates, slags, and cement were mixed in a container for 300s. Additives like GGBS or SS were added gradually after the first 30s to promise even distribution. Meanwhile, the processed GP solution with SP was divided into two equal dosages. After the dry mixing, the first GP solution was sprayed over the dry mixture and stirred for another 80s period. Lastly, the remaining solution was blended into the aforementioned composites with a 200s mixing process to produce ECCC. For the casting procedure, the ECCC had to experience 30s vibration to eliminate the trapped bubbles according to the GB/T 50081-2002 [40]. Regarding curing conditions, moulded samples were transferred to a wet cabinet with humidity (95 ± 5%) and temperatures (20 ± 1 °C) for 24 h. Then, specimens were demoulded and stored in this cabinet for designated days like 7, 14, 21, and 28 days. To conduct electrical tests, these ECCC samples need to be air-dried for 2 days after curing. For the mixture design in this study, these three fillers were added solely or in combinations to investigate their individual and overall impacts on ECCC, with the total number at 35. With respect to the mixing form, a combined sample including 5% SS, 10% GGBS, and 2% GP is written as SS5GGBS10GP2 for researchers and readers to easily understand its filler proportions and memorize. Referring to the grouping proportion, SS and GGBS were designed ranging from 5% to 15% while GP was controlled between 2% and 6% to control their impacts [41,42]. In summary, the detailed experimental procedures and information for each sample were exhibited in Fig. 1 and Table 3 respectively.

2.1.3. *Electric conductivity and mechanical tests of ECCC*

A four-pole method was adopted for the resistance experiment to measure the electrical conductivity of ECCC. As shown in Fig. 2, specimens with the size of 100 × 100 × 400 mm were prepared, and the metal mesh was parallel to the cross-section and bonded uniformly to the surface of the specimen at 120 mm intervals. A digital multimeter was applied to record the resistance through the copper wires connected to meshes [41]. The electrical resistivity of ECCC was calculated.

$$\rho = \frac{UA}{IL} \tag{1}$$

where ρ is resistivity (Ω·m), A is the cross-section area of the specimen (m^2), U denotes the voltage in the unit of V and I represent electric current in the unit of A.

The compressive and flexural tests of ECCC with different curing ages (7, 14, and 28 days) were performed to verify the influence of the conductive fillers on the mechanical

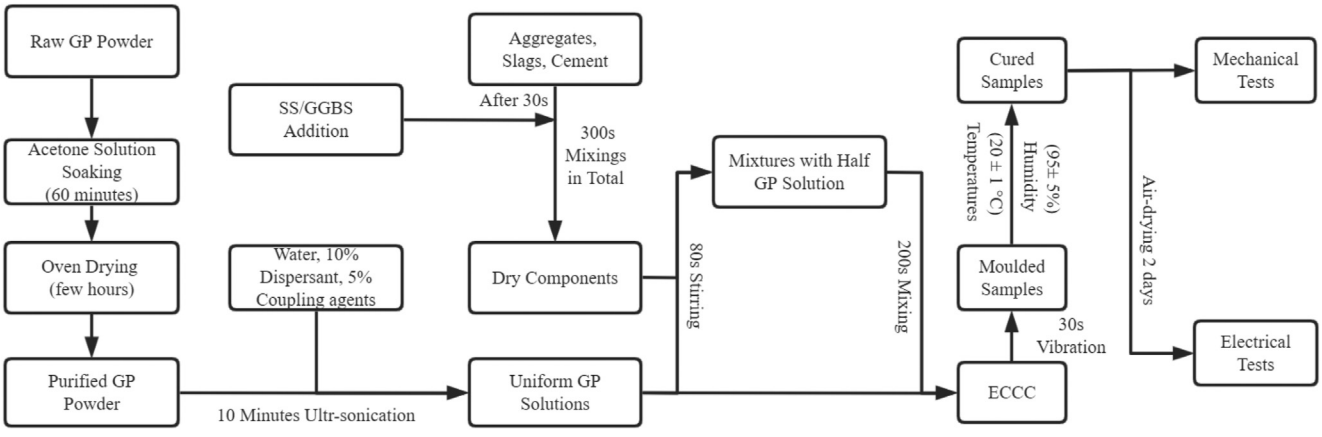

Fig. 1 – Overall experimental process for ECCC samples.

Table 3 – Mix design of ECCC with different fractions of conductive fillers.

Mix	OPC (kg/m^3)	CA (kg/m^3)	FA (kg/m^3)	Water (kg/m^3)	SP (kg/m^3)	SS (%)	GGBS (%)	GP (%)
Control	450	1302	884	160	1.42	0	0	0
SS5	427.5	1302	884	160	1.42	5	0	0
GGBS5	427.5	1302	884	160	1.42	0	5	0
GP5	427.5	1302	884	160	1.42	0	0	5
SS5GGBS5GP2	405	1302	884	160	1.42	5	5	2
SS5GGBS5GP4	405	1302	884	160	1.42	5	5	4
SS5GGBS5GP6	405	1302	884	160	1.42	5	5	6
SS5GGBS10GP2	382.5	1302	884	160	1.42	5	10	2
SS5GGBS10GP4	382.5	1302	884	160	1.42	5	10	4
SS5GGBS10GP6	382.5	1302	884	160	1.42	5	10	6
SS5GGBS15GP2	360	1302	884	160	1.42	5	15	2
SS5GGBS15GP4	360	1302	884	160	1.42	5	15	4
SS5GGBS15GP6	360	1302	884	160	1.42	5	15	6
SS10GGBS5GP2	382.5	1302	884	160	1.42	10	5	2
SS10GGBS5GP4	382.5	1302	884	160	1.42	10	5	4
SS10GGBS5GP6	382.5	1302	884	160	1.42	10	5	6
SS10GGBS10GP2	360	1302	884	160	1.42	10	10	2
SS10GGBS10GP4	360	1302	884	160	1.42	10	10	4
SS10GGBS10GP6	360	1302	884	160	1.42	10	10	6
SS10GGBS15GP2	337.5	1302	884	160	1.42	10	15	2
SS10GGBS15GP4	337.5	1302	884	160	1.42	10	15	4
SS10GGBS15GP6	337.5	1302	884	160	1.42	10	15	6
SS15GGBS5GP2	360	1302	884	160	1.42	15	5	2
SS15GGBS5GP4	360	1302	884	160	1.42	15	5	4
SS15GGBS5GP6	360	1302	884	160	1.42	15	5	6
SS15GGBS10GP2	337.5	1302	884	160	1.42	15	10	2
SS15GGBS10GP4	337.5	1302	884	160	1.42	15	10	4
SS15GGBS10GP6	337.5	1302	884	160	1.42	15	10	6
SS15GGBS15GP2	315	1302	884	160	1.42	15	15	2
SS15GGBS15GP4	315	1302	884	160	1.42	15	15	4
SS15GGBS15GP6	315	1302	884	160	1.42	15	15	6
SS1GP4	445.5	1302	884	160	1.42	1	0	4
SS2GP3	441	1302	884	160	1.42	2	0	3
SS3GP2	436.5	1302	884	160	1.42	3	0	2
SS4GP1	432	1302	884	160	1.42	4	0	1

performance [40,43,44]. Specimens with the size of 50 × 50 × 50 mm and 50 × 50 × 200 mm were prepared for compressive tests and flexural tests, respectively. A 2000 kN digital servo-hydraulic universal testing machine (MTS YAW-4206, USA) was employed, giving a loading rate of 0.6 MPa/s for the uniaxial compression test and 0.03 MPa/s for the flexural test until failure. At least 5 specimens were tested for each batch of mix design, from which the average value was taken as compressive strength and flexural strength.

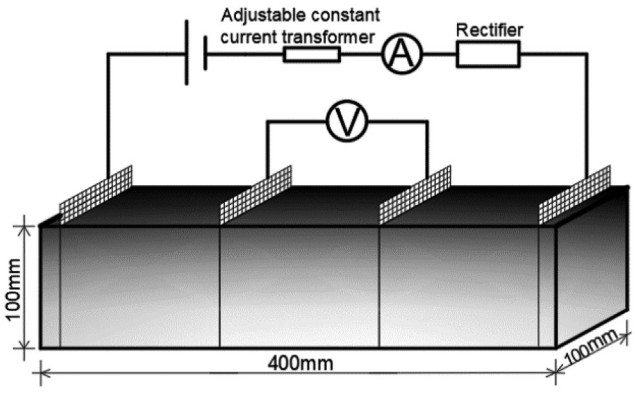

Fig. 2 – Illustration of the electric conductivity test of ECCC [27].

2.2. *Molecular dynamic simulation*

MD simulations were conducted to investigate the interfacial properties of conductive fillers in ECCC. Considering the conductive fillers: GP, SS, and GGBS, consist of various chemical components, such as graphite, SiO_2, Al_2O_3, and Fe_2O_3, multiple interfaces exist between these fillers and cement at the molecular scale. Therefore, four MD simulation models were constructed, namely graphite-CSH (GCSH), Fe_2O_3-CSH (FCSH), Al_2O_3-CSH (ACSH), and SiO_2-CSH (SCSH), where CSH (calcium silicate hydrates), as the main hydration product of cement, was used to represent cement matrix. As shown in Fig. 3, period simulation boxes were created ($a = 53.1$ Å, $b = 24.8$ Å, $c = 55.9$ Å, and $\alpha = 90°$, $\beta = 90°$, $\gamma = 88.6°$) by placing CSH of 14 Å tobermorite [45] on the top of substrates, namely, graphite, Al_2O_3, Fe_2O_3, and SiO_2. The mismatch rates of CSH and all substrates were kept at less than 5% to avoid crashing the systems.

Following an energy minimization, all MD models proceeded with a 20ps isothermal-isobaric (NPT) ensemble at 300 K and atmospheric pressure with a time step of 1×10^{-4} ps

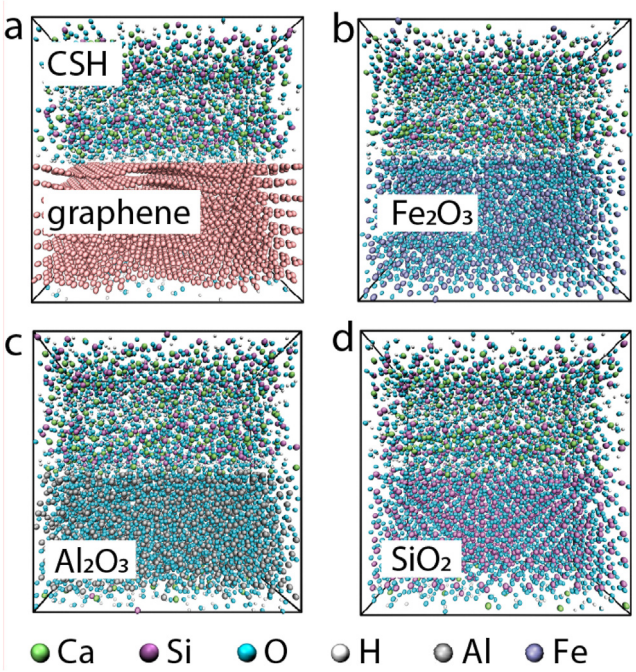

Fig. 3 – Illustration of the MD simulation model of (a) GCSH, (b) ACSH (CSH–Al_2O_3), (c) FCSH and (d) SCSH.

to allow for cell relaxation and minimize the system pressure. The atomic interactions were modeled by a reactive force field [46,47], which can simulate the breaking and reformation of the chemical bonds. Parameters of this force field were obtained from previous studies that show a good agreement in the systems containing C, H, Ca, Si, Al, and Fe [48–50]. After the NPT ensemble, shear loading was applied by dilating the simulation cell along the shear direction (x-direction) at a constant rate and simultaneously adjusting the atoms' positions and velocities based on canonical (NVT) to keep the equilibrium of the systems. The displacements of the atoms at the top of the simulation cell were around 1 Å/ps at a time step of 2.5×10^{-4} ps, leaving enough relaxing time to avoid temperature accumulation in the local area. Stress distribution was calculated based on the Virial theorem [51–53], and visual molecular dynamic (VMD) was applied to visualize the simulation process.

3. Results and discussion

3.1. *Results of electric conductivity and mechanical test*

Fig. 4 depicts the impacts of each conductive additive on ECCC behaviours in mechanical and resistivity aspects. Compared with the parent specimen, 5% SS addition improved the strengths of concrete, from 57.5 to 60.7 MPa (5.6%) in compressive and from 3.9 to 4.31 MPa (10.5%) in flexural aspects after 28 days of curing. The explanation was that tiny SS particles (0.5–1 μm) could fill pores in cement and therefore provide a massive interaction area with components in concrete, enhancing the mechanical properties of ECCC [35,54]. Unlike SS, GGBS and GP were proved to weaken the mechanical strengths of ECCC to different extents in this study. From Fig. 4(a) and (b), the sample prepared with 5% GGBS owned 55.9 and 3.8 MPa in compressive and flexural performance respectively, lower than the 57.5 and 3.9 MPa of the control specimen. This decreasing trend of GGBS was more likely caused by two possible reasons, in contrast to the increasing tendency of SS having similar major components. One possible explanation is its less Fe_2O_3 content (1.8%), which could undertake external load in the experimental process based on MD results. Another reason is the larger particle size of GGBS, leading to the decreasing contact area. Moreover, GGBS has the slow hydration characteristic that developed final strengths after 28 days [55,56]. As for the GP impact, it was clear that the 5% GP destroyed the strengths of ECCC, decreasing to 44.6 (28.9%) and 3.04 MPa (28.2%). This phenomenon was attributed to the smooth micro-structural surface of GP, lubricating and weakening the bonding relationship between aggregates and interfacial transition zone (ITZ) [57].

Referring to the resistivity aspect, all three conductive fillers enhanced the electrical conductivity of the ECCC. From Fig. 4 (c), SS and GGBS reduced the resistance efficiently from the original 4205411 Ω cm to 315907 (92.5%) and 642626 Ω cm (84.7%) respectively when fully cured. Metal oxides of these two additives could be responsible for the conductivity promotion efficiency of ECCC samples. As for the GP, it behaved outstandingly among three conductive fillers in the conductivity aspect, lowering resistance to 94128 Ω cm (97.8%). The substantial improvement caused by GP addition in electrical conductivity came from two aspects. One is the great conductivity of GP itself, and another is the formation of the GP network [58].

Although the influence of sole filler addition was determined, the overall impact of combined conductive additives was still uncertain. To demonstrate it, a series of samples involving SS, GGBS, as well as GP, were prepared as mentioned above, and their corresponding results were described in Fig. 5. From Fig. 5(a), the sample prepared with 5% SS and 5% GGBS owned 54.5 and 4.3 MPa for UCS as well as FS value at 2% GP, which dropped to 44.7 and 3.41 MPa under 6% GP mixture. And the increase in GP also reduced the resistivity sharply from 612034 Ω cm (2% GP) to 82431 Ω cm (6% GP). As for GGBS, a 5% increment of GGBS between 5% and 10% resulted in the UCS declining from 46.28 to 43.58 MPa, and the FS dropping from 3.95 to 3.84 MPa at 2% GP and 15% SS status from Fig. 5(c). It also reduced the electrical resistance of ECCC from 284563 to 224366 Ω cm when its proportion rose from 10% to 15%. Both GP and GGBS verified the aforementioned conclusions derived from Fig. 4. However, samples involving 2% GP and 5% GGBS experienced strength reductions from 54.54 (5% SS) to 46.28 MPa (15% SS) in UCS and from 4.3 (5% SS) to 3.95 Mpa (15% SS) in FS aspects, according to Fig. 5. This opposite conclusion was caused by excessive SS content (15%), which replaced cement clinker and therefore decreased reaction products to impair the performances of concrete samples [59,60].

To explore the significance of filler content, several ECCC samples were produced from limited conductive additives that were within 5% cement clinker replacement in total, and their results were plotted in Fig. 6. Among these samples, SS was added instead of GGBS because it had greater efficiency in ECCC performances on the basis of similar mineral

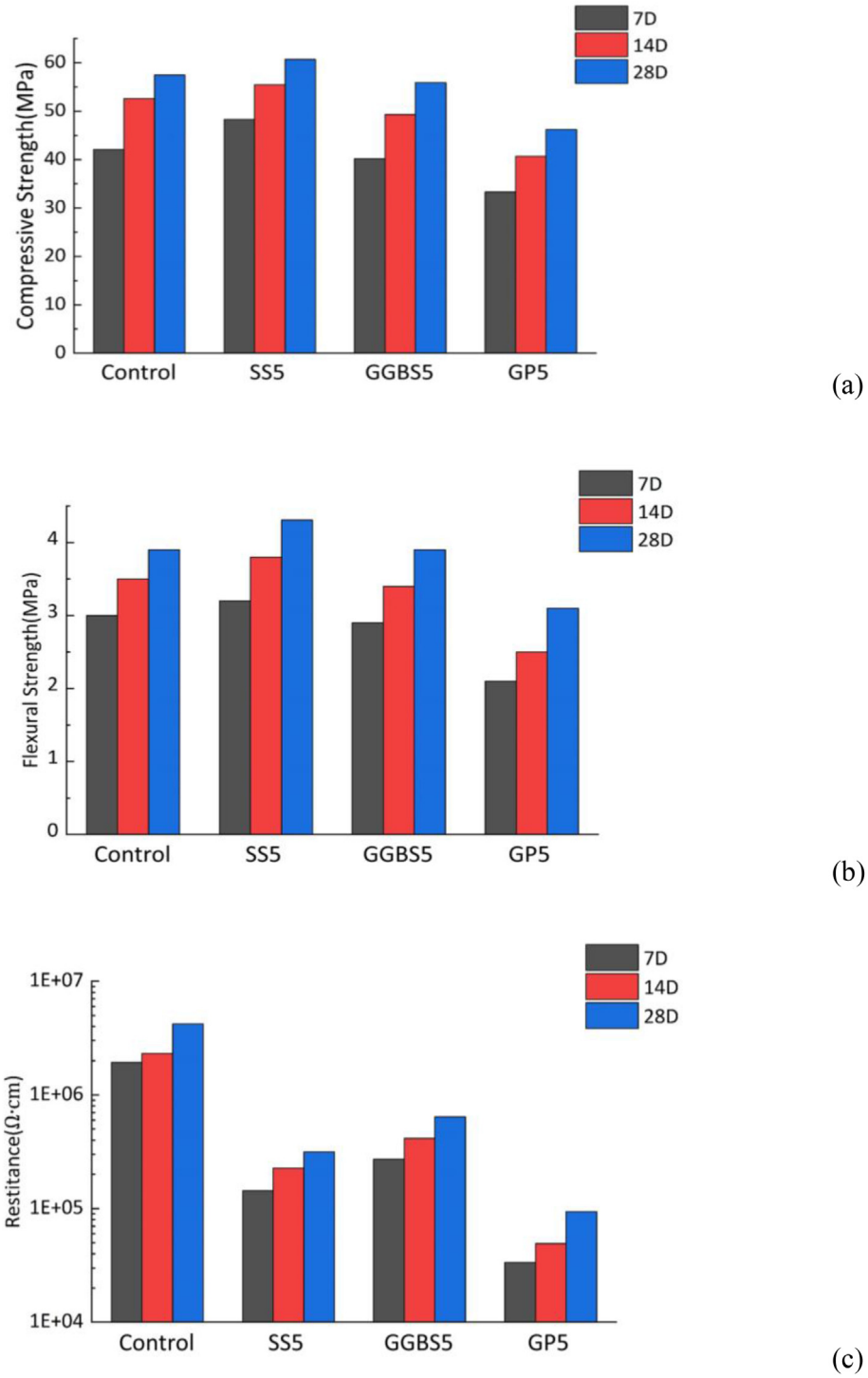

Fig. 4 – Diagrams for influences of individual conductive fillers on performances of ECCC samples (a) UCS performance (b) FS performance (c) Resistivity performance.

components. It is noted that the high efficiency of GP exhibited a degradation trend along with its decreasing content. From Fig. 6(c), the resistance of ECCC experienced a sharp increase from 1.3×10^5 Ω•cm (SS1GP4) to 1.5×10^6 Ω•cm (SS2GP3) and then rose slightly to 3.1×10^6 Ω•cm (SS4GP1). The threshold of 4% GP existing in ECCC conductivity promotion may come from the GP network development.

3.2. *Results of molecular dynamic simulation*

3.2.1. *Interfacial properties of the conductive fillers in cementitious composites at the molecular level*

The shear strength (σ_s) at the interface between filers and cement, as one of the interfacial properties, played a significant role in the mechanical performance of ECCC [61]. When

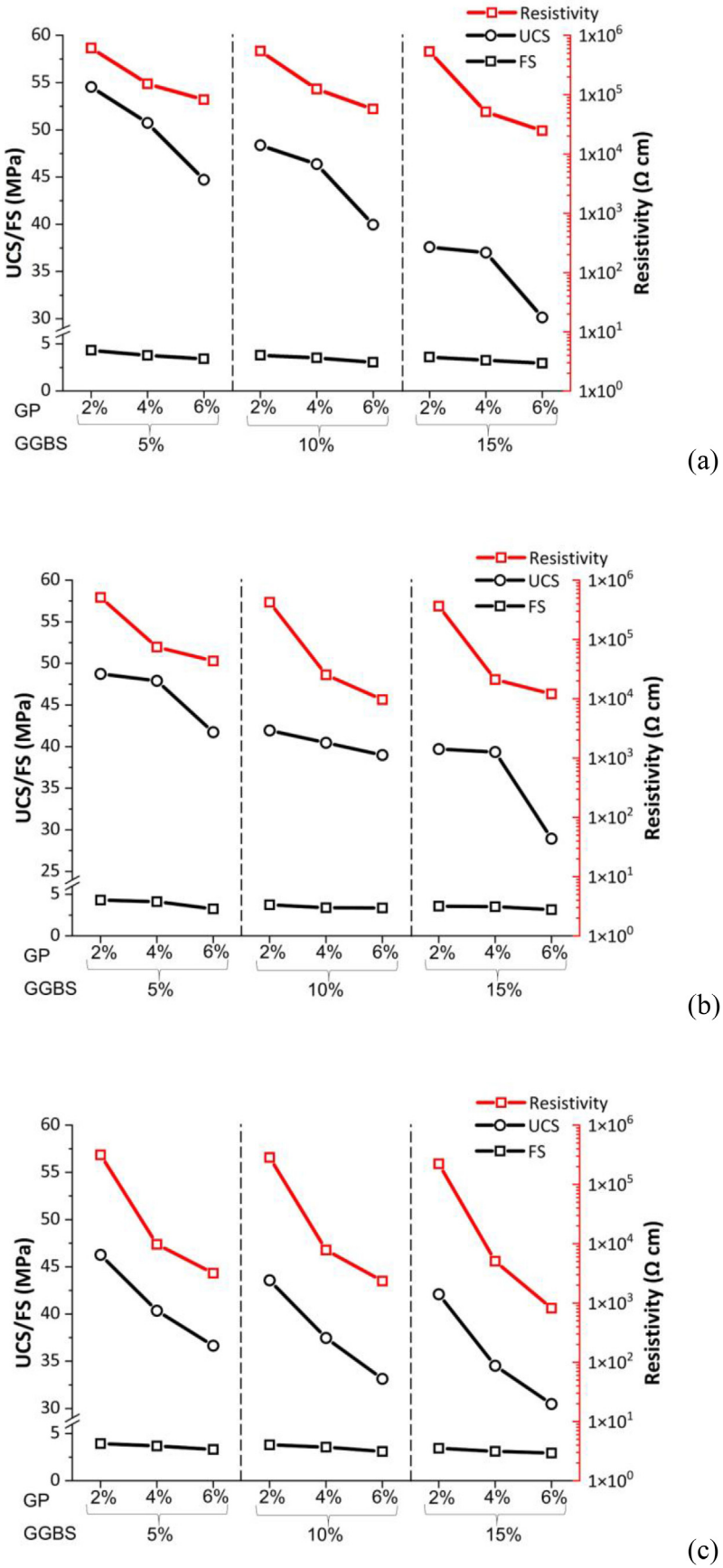

Fig. 5 – Diagrams for the influences of combined additives on mechanical and conductive performances of ECCC samples (a) SS-5% (b) SS-10% (c) SS-15%.

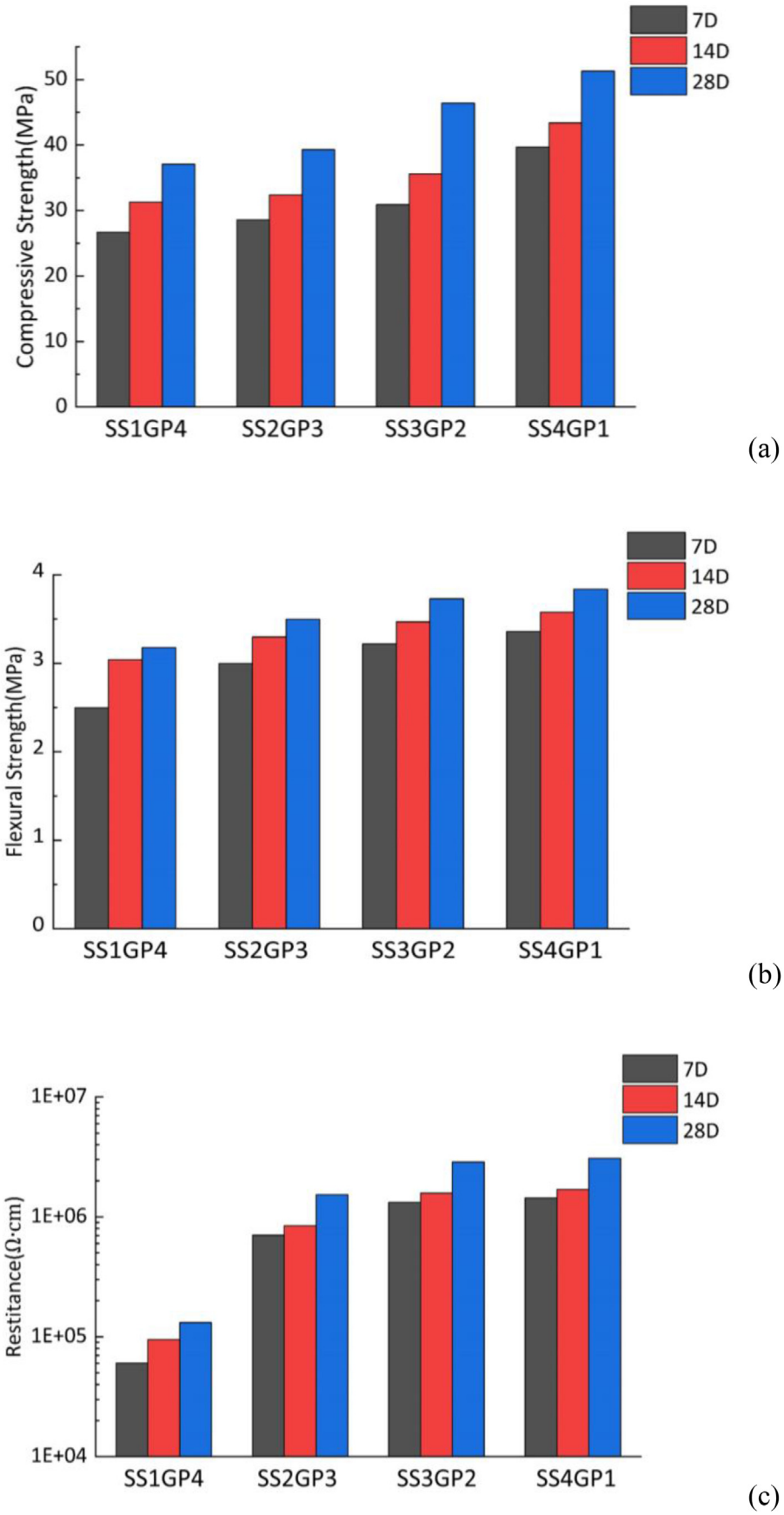

Fig. 6 – Diagrams for influences of two conductive fillers on performances of ECCC samples.

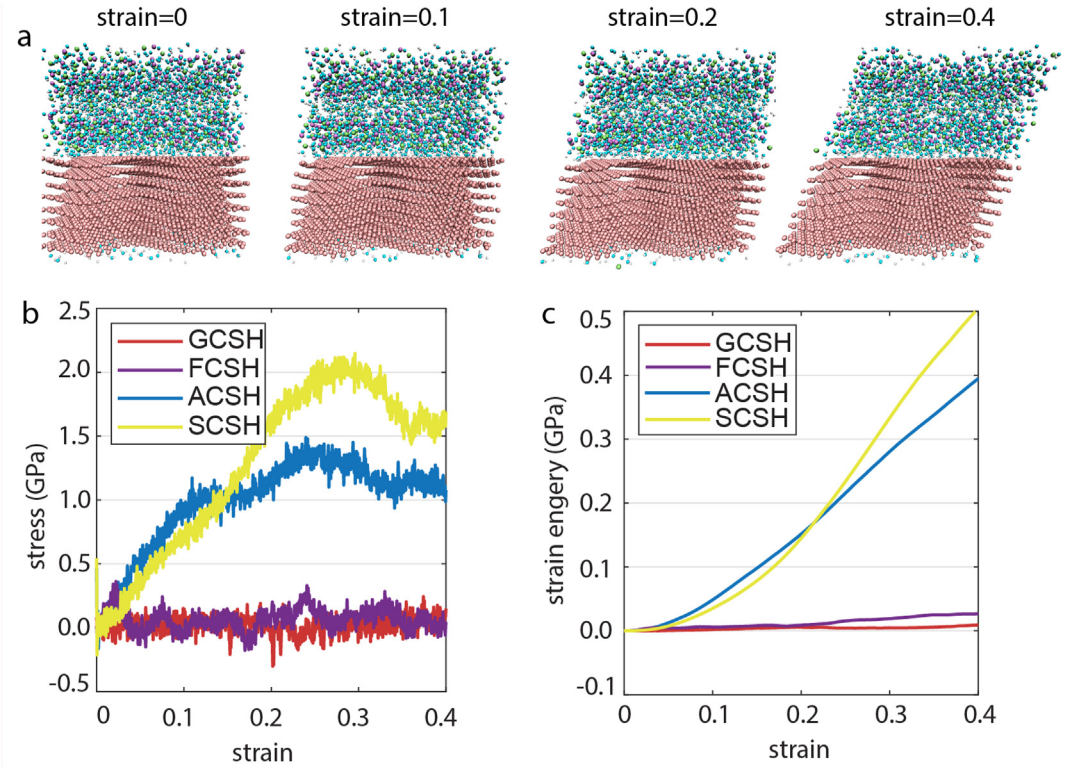

Fig. 7 – (a) Illustration of the shearing test in MD simulation. (b) Shear response and (c) strain energy of different MD models under shear strain.

ECCC is subjected to compressive or flexural load, cracks form and propagate through the interface between fillers and cement, inducing shear deformation and shear stress [62,63]. Therefore, in this study, shear tests performed in MD simulation were employed to investigate the response of the interface between conductive fillers (GP, SS, and GGBS) and cement matrices at the molecular scale. Because SS and GGBS have complex mineral components, such as Al_2O_3, Fe_2O_3, SiO_2,

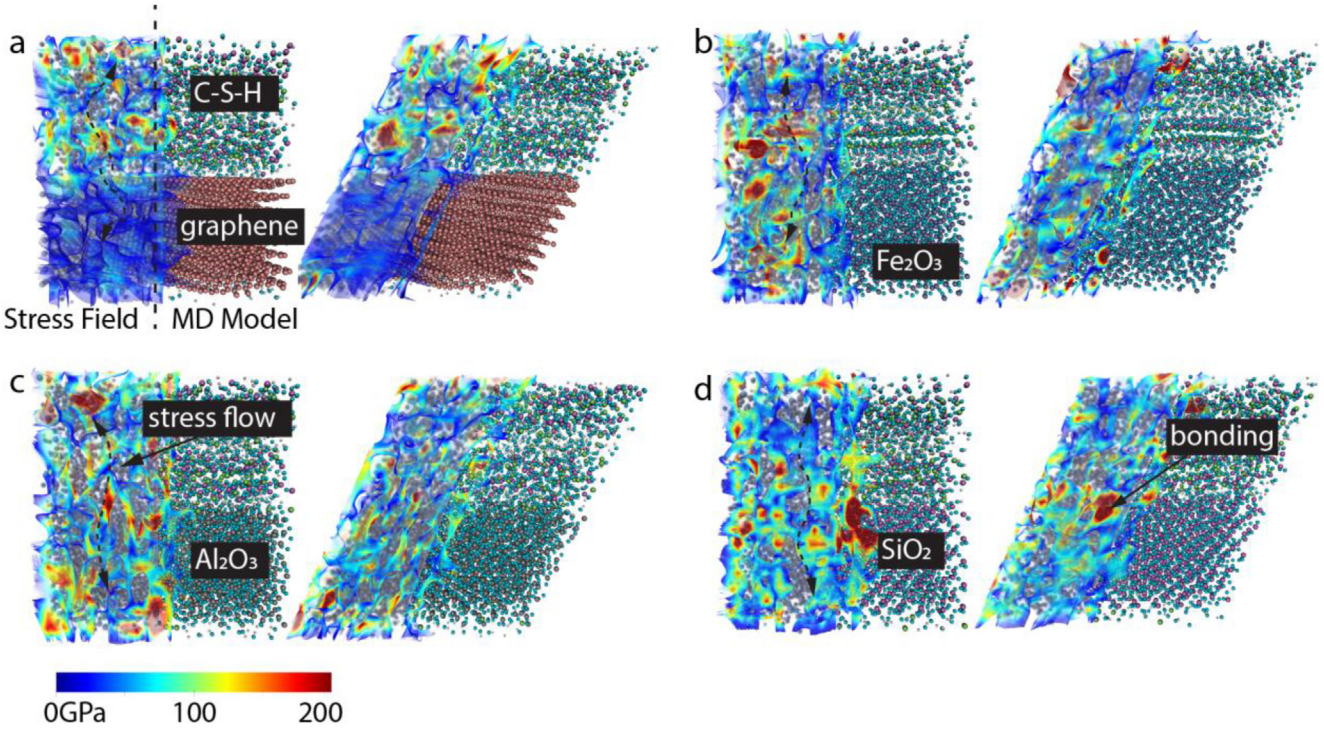

Fig. 8 – Stress flow in (a) GCSH, (b) FCSH, (c) ACSH and (d) SCSH under shear strain of 0 and 0.4 during MD simulation.

as shown in Table 1, the insight into the slags' interface with cement matrix at a molecular scale was conducted by studying the interface of each of their mineral components with CSH (main components of cement hydrates representing cement matrix). Therefore, including graphite, four targeted MD simulation models were constructed: CSH with graphite (GCSH), CSH with Al_2O_3 (ACSH), CSH with Fe_2O_3 (FCSH) and CSH with SiO_2 (SCSH).

The process of the shearing test conducted for the GCSH model at different shear strains is illustrated in Fig. 7(a). Shear strain is defined as $\Delta x/h$, where Δx is the displacement of the top atoms and h is the height of the simulation box. A similar shearing process was also repeated in ACSH, FCSH, and SCSH systems, and the corresponding mechanical response was collected.

As shown in Fig. 7(b), SCSH possesses the highest σ_s (maximum value of stress) of all MD models in this loading configuration. After reaching the peak at around 2.1 GPa, the stress of SCSH decreased significantly to less than 1.6 GPa with the strain continuing to increase from 0.3 to 0.4. This decrease is mainly caused by the break of strong interfacial bonding between SiO_2 and CSH at high shear strain. Similarly, the stress of ACSH also rises gradually with the strain until reaching around 1.4 GPa. Then, about 16.7% reduction of stress is observed when strain further increases to 0.4. Compared with SCSH, the reduction of stress after the peak is much smaller in ACSH. This is because the interfacial bonding between Al_2O_3 and CSH is weaker than its counterpart between SiO_2 and CSH. On the other hand, because of the weak interaction of graphite with CSH [64–66], the σ_s of GCSH in this MD simulation is only around 0.3 GPa, which is much smaller than those in SCSH and ACSH. This result verified the conclusion that GP behaved worse than the other two conductive fillers.

To gain a deeper understanding of the shear response at the interface of graphite and slags with CSH, stress flows of GCSH, ACSH, FCSH, and SCSH were calculated from the Cauchy stress tensor, plotted in Fig. 8. In terms of GCSH, because the interlayer in graphite is mainly connected by Van de Walls force [67,68], sliding between the layers can easily occur, which makes the graphite substrate in GCSH has limited effects in resisting the shear deformation. Therefore, as illustrated in Fig. 8(a), the shear load is mainly carried by the CSH structure itself. On the contrary, in terms of FCSH, shown in Fig. 8(b), besides CSH, Fe_2O_3 can effectively resist the shear deformation [69,70], thereby large stress was subjected to the Fe_2O_3 substrate. This conclusion conforms to the mechanical performances of GGBS samples having less Fe_2O_3 content (1.8%) than that of SS (21.3%) from Figures Fig. 4(a) and (b). However, as shear deformation continues growing with time, stress at the interface between Fe_2O_3 and CSH reduced rapidly, which indicates a weak interfacial bonding of Fe_2O_3 and CSH. On the other hand, for ACSH and SCSH, besides the substrates carrying a large amount of high shear stress, great stress was noticed at the interface, especially between CSH and SiO_2. This strong interfacial bonding between CSH and Al_2O_3 or SiO_2 contributed remarkably to resisting the shear deformation, which also explained the reason why the σ_s of ACSH and SCSH more than 2.9 and 4.8 times higher than that of FCSH.

3.2.2. *Impact of the conductive fillers on surrounding cementitious matrix*

To gain a comprehensive understanding of the interfacial properties, apart from the mechanical shear strength, the impact of the interfacial interaction on the cement matrix in the fillers' vicinity was also investigated. At the molecular level, the structure of CSH at the conductive fillers' vicinity was studied by using MD simulation. Fig. 9(a) shows the intensity distribution of CSH after the NPT ensemble in the MD simulation, where the contact surface between CSH and the substrates (graphite, Fe_2O_3, Al_2O_3, and Fe_2O_3) was normalized at 0 in the z-direction. Compared to FCSH and ACSH, a 2 times wider interphase (the zone where CSH and the substrates penetrated each other) is noticed in SCSH, which suggested a stronger interaction between SiO_2 and CSH. On the other hand, the weak interaction between graphite and CSH led to smaller interphase, which also contributed to the low value of σ_s. To further investigate the interphase between CSH and the substrates, radial distribution functions (RDF) were calculated by using: Eq. (2) [71,72].

$$g(r) = \frac{1}{N}\frac{dn(r)}{4\pi r^2 dr} \tag{2}$$

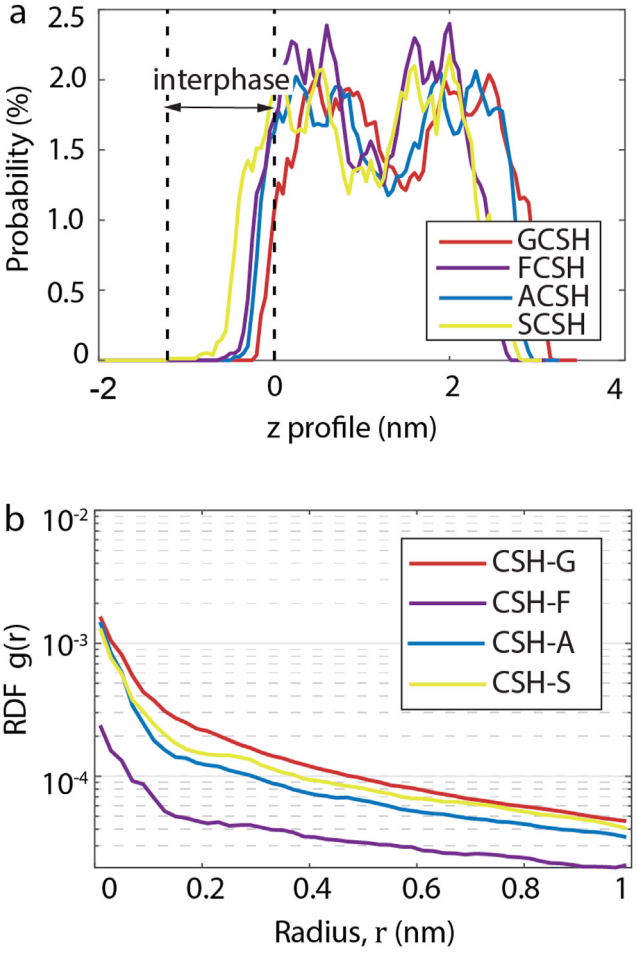

Fig. 9 – (a) Distribution of CSH in the z-direction, in different MD models. (b) Radial distribution function (RDF) of CSH and H_w to graphite (CSH-G, H_w-G), Al_2O_3 (CSH-A, H_w-A), Fe_2O_3 (CSH–F, H_w-G), and SiO_2 (CSH-G, H_w-G).

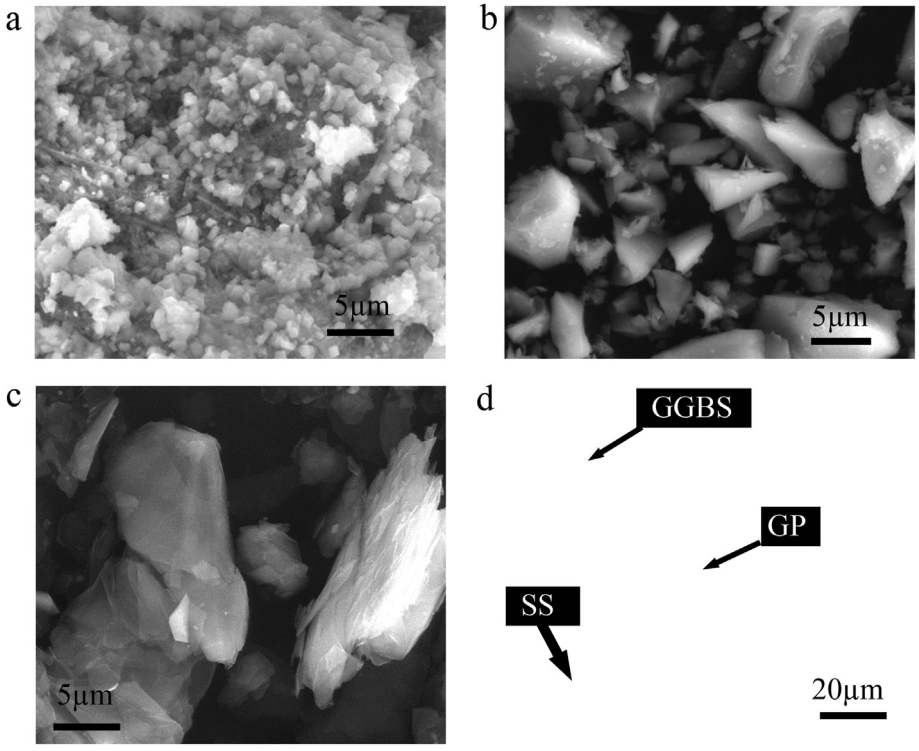

Fig. 10 – (a–d) Surface morphologies of (a) SS, (b) GGBS, (c) GP, and (d) ECCC mixed with conductive fillers.

where N is the total number of atoms of C–S–H adjacent mineral nanoparticles; r is the distance between C–S–H atoms and mineral nanoparticle atoms, and $dn(r)$ is a function that computes the number of adjacent atoms within a shell thickness of dr (0.01 nm).

As shown in Fig. 9(b), the general value of RDF of CSH with Al_2O_3 (CSH-A) and SiO_2 (CSH–S) is about 2.1 and 2.4 times higher than that of CSH with Fe_2O_3 (CSH–F), respectively. The large value of RDF indicates a stronger spatial correlation between CSH and SiO_2 or Al_2O_3 in comparison with CSH with Fe_2O_3, which accounts for the strong interfacial interactions. However, it is also noticed that the RDF of CSH with graphite is unexpectedly high, which was generally 30.5% higher than that of CSH with SiO_2. Because different from Fe_2O_3, Al_2O_3, and SiO_2 minerals, graphene (components of graphite) shows ultra-high flexibility [73–75]. Consequently, this high flexibility leads to a ripple-like surface morphology of graphite at its interface with CSH [76], which results in a high value of CSH-G.

3.3. *SEM analysis*

Besides the MD simulation investigating the interphase at the molecular level, the microstructure of cement matrix at the conductive fillers' vicinity was also viewed in SEM. As shown in Fig. 10(a–b), SS and GGBS equip massive square crystals of sharp edges with the size around 0.5–1 μm and 5–10 μm, respectively. However, the morphology of GP (Fig. 10(c)) shows a planar structure with hierarchical layers. Therefore, due to their various morphologies, conductivity fillers: SS, GGBS, and GP, can be identified in the cement matrix, as shown in Fig. 9(d). Owing to the high content of Fe_2O_3, Al_2O_3, and SiO_2 mineral components, SS or GGBS have a strong interaction with cement, facilitating the formation of cement hydrates in their vicinity [77–79]. On the other hand, the weak interaction between GP and cement leads to a weak interfacial bonding with less hydration product formed around GP. These findings showed a good consistency of our MD simulation results, where Fe_2O_3, Al_2O_3, and SiO_2 mineral components showed a much stronger interaction with CSH than graphite.

4. Conclusion

In the present study, for the first time, the interfacial properties of graphite particles (GP) and two waste slags: steel slags (SS) and ground granulated blast furnace slag (GGBS), were studied at the molecular level. A framework was proposed connecting these interfacial properties with the engineering performance of electrically conductive cementitious composites (ECCC). Based on the results from both molecular dynamic (MD) simulation and experiments, key findings can be summarised as follows:

(1) The mechanical properties of ECCC with conductive fillers were measured by the compressive test and flexural test. Incorporation of 5% SS improved 5.6% compressive strength and 10.5% flexural strength. On the other hand, a load of 5% GP degraded 28.9% compressive strength and 28.2% flexural strength.
(2) The electrical conductivity of ECCC was improved significantly by GP, SS, and GGBS by reducing 97.8%,

92.5%, and 84.7% of the resistance. This improvement not only attributed to the conductivity of GP, SS, and GGBS, the formation of a network of these fillers in ECCC also enhanced the conductive performance of ECCC significantly.

(3) The MD simulation revealed that the mineral components of conductive fillers played a significant role in the shear strength at the interface. The σ_s in graphite-CSH (GCSH) is more than 19.4%, 80.4% and 86.4% lower than that in Fe_2O_3-CSH (FCSH), Al_2O_3-CSH (ACSH), and SiO_2-CSH (SCSH), respectively, where CSH represents calcium silicate hydrates. Further analysis of the shear stress distribution indicates that this low value of σ_s in GCSH is attributed to the combination of the weak interlayer shear strength within graphite and the weak interfacial bonding between graphite and CSH.

(4) The impact of conductive fillers on their surrounding cement was studied by observation of the microstructure in SEM. Compared with GP, the growth of cement hydrates was facilitated around SS and GGBS, suggesting a stronger interaction between SS or GGBS with cement. MD simulation results show that this strong interaction is mainly attributed to the mineral components, such as Fe_2O_3, Al_2O_3, and SiO_2 in SS or GGBS.

In summary, although the incorporation of GP enhanced the electrical conductivity of ECCC remarkably, the mechanical properties of ECCC were degraded. This degradation of mechanical properties can be offset by introducing SS in the ECCC system. Therefore, the fundamental understanding of the role of conductive fillers played at the molecular level in ECCC shown in this paper can pave a way for designing high-performance ECCC.

Compliance with ethical standards

Research involving human participants and/or animals

This article does not contain any studies with human participants or animals performed by any of the authors.

Informed consent

Not applicable.

Funding details

This study was funded by Natural Science Foundation of Guangxi Province (grant number 2021GXNSFAA220045); China Postdoctoral Science Foundation (grant number 2021M690765); Systematic Project of Guangxi Key Laboratory of Disaster Prevention and Engineering Safety (grant number 2021ZDK007); Academic Research Council of Australia Linkage Projects for Asset Intelligence: Maximising Operational Effectiveness for Digital Era (grant number LP180100222); State Key Laboratory for GeoMechanics and Deep Underground Engineering, China University of Mining & Technology/China University of Mining & Technology, Beijing (SKLGDUEK2105).

Declaration of Competing Interest

The authors declare that they have no known competing financial interests or personal relationships that could have appeared to influence the work reported in this paper.

REFERENCES

[1] Miller SA, John VM, Pacca SA, Horvath A. Carbon dioxide reduction potential in the global cement industry by 2050. Cement Concr Res 2018;114:115–24.

[2] Sun J, Huang Y, Aslani F, Wang X, Ma G. Mechanical enhancement for EMW-absorbing cementitious material using 3D concrete printing. J Build Eng 2021:102763.

[3] Xu S, Wang J, Shou W, Ngo T, Sadick AM, Wang X. Computer vision techniques in construction: a critical review. Arch Comput Methods Eng 2021;28(5):3383–97.

[4] Zhang W, Tang Z. Numerical modeling of response of CFRP–concrete interfaces subjected to fatigue loading. J Compos Construct 2021;25(5):04021043. https://doi.org/10.1061/(ASCE)CC.1943-5614.0001154.

[5] Hou L, Wu S, Zhang GK, Tan Y, Wang X. Literature review of digital twins applications in construction workforce safety. Appl Sci 2021;11(1):339.

[6] Huang H, Xue C, Zhang W, Guo M. Torsion design of CFRP-CFST columns using a data-driven optimization approach. Eng Struct 2022;251:113479. https://doi.org/10.1016/j.engstruct.2021.113479.

[7] Barcelo L, Kline J, Walenta G, Gartner E. Cement and carbon emissions. Mater Struct 2014;47(6):1055–65.

[8] Tong X, Zhang F, Ji B, Sheng M, Tang Y. Carbon-coated porous aluminum foil anode for high-rate, long-term cycling stability, and high energy density dual-ion batteries. Adv Mater 2016;28(45):9979–85. https://doi.org/10.1002/adma.201603735.

[9] Wang L, Yuan J, Wu C, Wang X. Practical algorithm for stochastic optimal control problem about microbial fermentation in batch culture. Optimization Letters 2019;13(3):527–41.

[10] Feng W, Wang Y, Sun J, Tang Y, Wu D, Jiang Z, et al. Prediction of thermo-mechanical properties of rubber-modified recycled aggregate concrete. Construc Build Mater 2022;318:125970.

[11] Sun J, Tang Y, Wang J, Wang X, Wang J, Yu Z, et al. A multi-objective optimisation approach for activity excitation of waste glass mortar. J Mater Res Technol 2022;17:2280–304.

[12] Sun J, Wang Y, Liu S, Dehghani A, Xiang X, Wei J, et al. Mechanical, chemical and hydrothermal activation for waste glass reinforced cement. Construct Build Mater 2021;301:124361.

[13] Sun J, Wang J, Zhu Z, He R, Peng C, Zhang C, et al. Mechanical performance prediction for sustainable high-strength concrete using bio-inspired neural network. Buildings 2022;12(1):65.

[14] Tang Y, Feng W, Chen Z, Nong Y, Guan S, Sun J. Fracture behavior of a sustainable material: recycled concrete with waste crumb rubber subjected to elevated temperatures. J Clean Product 2021;318:128553.

[15] Zhang G, Chen C, Li K, Xiao F, Sun J, Wang Y, et al. Multi-objective optimisation design for GFRP tendon reinforced cemented soil. Construct Build Mater 2022;320:126297.

[16] Sun J, Ma Y, Li J, Zhang J, Ren Z, Wang X. Machine learning-aided design and prediction of cementitious composites

containing graphite and slag powder. J Build Eng 2021;43:102544.
[17] Sun J, Wang X, Zhang J, Xiao F, Sun Y, Ren Z, et al. Multi-objective optimisation of a graphite-slag conductive composite applying a BAS-SVR based model. J Build Eng 2021;44:103223.
[18] Wu C, Wang X, Chen M, Kim MJ. Differential received signal strength based RFID positioning for construction equipment tracking. Adv Eng Inf 2019;42:100960.
[19] Tsai Y-H, Wang J, Chien W-T, Wei C-Y, Wang X, Hsieh S-H. A BIM-based approach for predicting corrosion under insulation. Autom ConStruct 2019;107:102923.
[20] Lu N, Wang H, Wang K, Liu Y. Maximum probabilistic and dynamic traffic load effects on short-to-medium span bridges. Comput Model Eng Sci 2021;127:345–60. https://doi.org/10.32604/cmes.2021.013792.
[21] Wang L, Aslani FJC, Materials B. A review on material design, performance, and practical application of electrically conductive cementitious composites. Construct Build Mater 2019;229:116892.
[22] Singh V, Gu N, Wang X. A theoretical framework of a BIM-based multi-disciplinary collaboration platform. Autom ConStruct 2011;20(2):134–44.
[23] Zhang C, Jin Q, Song Y, Wang J, Sun L, Liu H, et al. Vibration analysis of a sandwich cylindrical shell in hygrothermal environment. Nanotechnol Rev 2021;10(1):414–30. https://doi.org/10.1515/ntrev-2021-0026.
[24] Zhao S, Zhang Y, Yang J, Kitipornchai S. Improving interfacial shear strength between graphene sheets by strain-induced wrinkles. Carbon 2020;168:135–43.
[25] Liu Z, Zhang S-M, Yang J-R, Liu JZ, Yang Y-L, Zheng Q-S. Interlayer shear strength of single crystalline graphite. Acta Mech Sin 2012;28(4):978–82.
[26] Wu C, Wang X, Wu P, Wang J, Jiang R, Chen M, et al. Hybrid deep learning model for automating constraint modelling in advanced working packaging. Autom ConStruct 2021;127:103733.
[27] Sun J, Lin S, Zhang G, Sun Y, Zhang J, Chen C, et al. The effect of graphite and slag on electrical and mechanical properties of electrically conductive cementitious composites. Construct Build Mater 2021;281:122606.
[28] Xie P, Gu P, Fu Y, Beaudoin J. Determination of blast-furnace slag content in hardened concrete by electrical conductivity methods. Cem Concr Aggregates 1995;17:79. 79.
[29] Xu D, Liu Q, Qin Y, Chen B. Analytical approach for crack identification of glass fiber reinforced polymer–sea sand concrete composite structures based on strain dissipations. Struct Health Monit 2020. https://doi.org/10.1177/1475921720974290.
[30] Wang M, Yang X, Wang W. Establishing a 3D aggregates database from X-ray CT scans of bulk concrete. Construct Build Mater 2022;315:125740. https://doi.org/10.1016/j.conbuildmat.2021.125740.
[31] Fang Q, Wang G, Yu F, Du J. Analytical algorithm for longitudinal deformation profile of a deep tunnel. J Rock Mech Geotech Eng 2021;13(4):845–54. https://doi.org/10.1016/j.jrmge.2021.01.012.
[32] Mou B, Bai Y. Experimental investigation on shear behavior of steel beam-to-CFST column connections with irregular panel zone. Eng Struct 2018;168:487–504. https://doi.org/10.1016/j.engstruct.2018.04.029.
[33] Xu D-s, Huang M, Zhou Y. One-dimensional compression behavior of calcareous sand and marine clay mixtures. Int J GeoMech 2020;20(9):4020137. https://doi.org/10.1061/(ASCE)GM.1943-5622.0001763.
[34] Yu Y, Yi X, Zhang J, Tong Z, Chen C, Ma M, et al. Application of ReOx/TiO2 catalysts with excellent SO2 tolerance for the selective catalytic reduction of NOx by NH3. Catal Sci Technol 2021;11(15):5125–34. https://doi.org/10.1039/D1CY00467K.
[35] Han B, Yu X, Ou J. Chapter 2 - compositions of self-sensing concrete. In: Han B, Yu X, Ou J, editors. Self-sensing concrete in smart structures. Butterworth-Heinemann; 2014. p. 13–43.
[36] Zhu J, Chen Y, Zhang L, Guo B, Fan G, Guan X, et al. Revealing the doping mechanism of barium in sulfoaluminate cement clinker phases. J Clean Prod 2021;295:126405. https://doi.org/10.1016/j.jclepro.2021.126405.
[37] Tan K, Qin Y, Du T, Li L, Zhang L, Wang J. Biochar from waste biomass as hygroscopic filler for pervious concrete to improve evaporative cooling performance. Construct Build Mater 2021;287:123078. https://doi.org/10.1016/j.conbuildmat.2021.123078.
[38] Standard A. AS 3972-1997 Portland and blended cements. Sydney: Standards Australia; 1997.
[39] Li J, Qin Q, Sun J, Ma Y, Li Q. Mechanical and conductive performance of electrically conductive cementitious composite using graphite, steel slag, and GGBS. Struct Concr 2020;23(1):533–47.
[40] Standard, C.. Gb/T, 50081-2002 Method for testing mechanical properties of normal concrete. 2002. Beijing, China.
[41] Baeza FJ, Galao O, Vegas I, Cano M, Garcés P. Influence of recycled slag aggregates on the conductivity and strain sensing capacity of carbon fiber reinforced cement mortars. Construct Build Mater 2018;184:311–9.
[42] Sun J, Huang Y, Aslani F, Ma G. Electromagnetic wave absorbing performance of 3D printed wave-shape copper solid cementitious element. Cement Concr Compos 2020:103789.
[43] Sun J, Aslani F, Wei J, Wang X. Electromagnetic absorption of copper fiber oriented composite using 3D printing. Construct Build Mater 2021;300:124026.
[44] Zhang W, Zhang R, Wu C, Goh ATC, Lacasse S, Liu Z, et al. State-of-the-art review of soft computing applications in underground excavations. Geosci Front 2020;11(4):1095–106.
[45] Bonaccorsi E, Merlino S, Kampf AR. The crystal structure of tobermorite 14 Å (plombierite), a C–S–H phase. J Am Ceram Soc 2005;88(3):505–12.
[46] Senftle TP, Hong S, Islam MM, Kylasa SB, Zheng Y, Shin YK, et al. The ReaxFF reactive force-field: development, applications and future directions. npj Computational Materials 2016;2(1):1–14.
[47] Zhang W, Li H, Li Y, Liu H, Ding X. Application of deep learning algorithms in geotechnical engineering: a short critical review. Artif Intell Rev 2021;(9):1–41.
[48] Psofogiannakis GM, McCleerey JF, Jaramillo E, van Duin AC. ReaxFF reactive molecular dynamics simulation of the hydration of Cu-SSZ-13 zeolite and the formation of Cu dimers. J Phys Chem C 2015;119(12):6678–86.
[49] Manzano H, Moeini S, Marinelli F, Van Duin AC, Ulm F-J, Pellenq RJ-M. Confined water dissociation in microporous defective silicates: mechanism, dipole distribution, and impact on substrate properties. J Am Chem Soc 2012;134(4):2208–15.
[50] Chenoweth K, Van Duin AC, Goddard WA. ReaxFF reactive force field for molecular dynamics simulations of hydrocarbon oxidation. J Phys Chem 2008;112(5):1040–53.
[51] Marc G, McMillan W. The virial theorem. Adv Chem Phys 1985;58:209–361.
[52] Tan L, Sun Y, Wei C, Tao Y, Tian Y, An Y, et al. Design of robust, lithiophilic, and flexible inorganic-polymer protective layer by separator engineering enables dendrite-free lithium metal batteries with LiNi0. 8Mn0. 1Co0. 1O2 cathode. Small 2021;17(13):2007717. https://doi.org/10.1002/smll.202007717.
[53] Zhang W, Wu C, Zhong H, Li Y, Wang L. Prediction of undrained shear strength using extreme gradient boosting

and random forest based on Bayesian optimization. Geosci Front 2021;12(1):469–77.
[54] Zhang R, Wu C, Goh AT, Böhlke T, Zhang W. Estimation of diaphragm wall deflections for deep braced excavation in anisotropic clays using ensemble learning. Geosci Front 2021;12(1):365–73.
[55] Kolani B, Buffo-Lacarrière L, Sellier A, Escadeillas G, Boutillon L, Linger LJC, et al. Hydration of slag-blended cements. Cem concre compos 2012;34(9):1009–18.
[56] Zhang W, Li H, Wu C, Li Y, Liu Z, Liu H. Soft computing approach for prediction of surface settlement induced by earth pressure balance shield tunneling. Undergr Space 2021;6(4):353–63.
[57] Janković K, Stanković S, Bojović D, Stojanović M, Antić LJC, Materials B. The influence of nano-silica and barite aggregate on properties of ultra high performance concrete. Construct Build Mater 2016;126:147–56.
[58] Jiao W, Sha A, Liu Z, Jiang W, Hu L, Li X. Utilization of steel slags to produce thermal conductive asphalt concretes for snow melting pavements. J Clean Prod 2020:121197.
[59] Maslehuddin M, Sharif AM, Shameem M, Ibrahim M, Barry MJC, materials b. Comparison of properties of steel slag and crushed limestone aggregate concretes. Construct Build Mater 2003;17(2):105–12.
[60] Anastasiou E, Filikas KG, Stefanidou MJC. Utilization of fine recycled aggregates in concrete with fly ash and steel slag. Bioact Mater 2014;50:154–61.
[61] Ju Y, Shen T, Wang D. Bonding behavior between reactive powder concrete and normal strength concrete. Construct Build Mater 2020;242:118024. https://doi.org/10.1016/j.conbuildmat.2020.118024.
[62] Anderson TL. Fracture mechanics: fundamentals and applications. CRC Press; 2017.
[63] Ouyang X, Ye G, van Breugel K. Experimental and numerical evaluation of mechanical properties of interface between filler and hydration products. Construct Build Mater 2017;135:538–49.
[64] Peyvandi A, Soroushian P, Abdol N, Balachandra AM. Surface-modified graphite nanomaterials for improved reinforcement efficiency in cementitious paste. Carbon 2013;63:175–86.
[65] Sun J, Aslani F, Lu J, Wang L, Huang Y, Ma G. Fibre-reinforced lightweight engineered cementitious composites for 3D concrete printing. Ceram Int 2021;47(19):27107–21.
[66] Liu J, Wu C, Wu G, Wang X. A novel differential search algorithm and applications for structure design. Appl Math Comput 2015;268:246–69.
[67] Liu Z, Liu JZ, Cheng Y, Li Z, Wang L, Zheng Q. Interlayer binding energy of graphite: a mesoscopic determination from deformation. Phys Rev B 2012;85(20):205418.
[68] Golkarian AR, Jabbarzadeh M. The density effect of van der Waals forces on the elastic modules in graphite layers. Comput Mater Sci 2013;74:138–42.
[69] Laanaiya M, Zaoui A. Preventing cement-based materials failure by embedding Fe2O3 nanoparticles. Construct Build Mater 2020;260:120466. https://doi.org/10.1016/j.conbuildmat.2020.120466.
[70] Hu J, Zhang H, Li Z, Zhao C, Xu Z, Pan Q. Object traversing by monocular UAV in outdoor environment. Asian J Control 2020. https://doi.org/10.1002/asjc.2415.
[71] Kuo I-FW, Mundy CJ. An ab initio molecular dynamics study of the aqueous liquid-vapor interface. Science 2004;303(5658):658–60.
[72] Hou D, Li T, Wang P. Molecular dynamics study on the structure and dynamics of NaCl solution transport in the nanometer channel of CASH gel. ACS Sustainable Chem Eng 2018;6(7):9498–509.
[73] Despres J, Daguerre E, Lafdi K. Flexibility of graphene layers in carbon nanotubes. Carbon Nanotub 1996;149:1–2.
[74] Chen F, Jin Z, Wang E, Wang L, Jiang Y, Guo P, et al. Relationship model between surface strain of concrete and expansion force of reinforcement rust. Sci Rep 2021;11(1):1–11. https://doi.org/10.1038/s41598-021-83376-w.
[75] Wang H, Memon H, AM Hassan E, Miah M, Ali M. Effect of jute fiber modification on mechanical properties of jute fiber composite. Materials 2019;12(8):1226.
[76] Fasolino A, Los J, Katsnelson MI. Intrinsic ripples in graphene. Nat Mater 2007;6(11):858–61.
[77] Heikal M, Zaki MEA, Ibrahim SM. Characterization, hydration, durability of nano-Fe2O3-composite cements subjected to sulphates and chlorides media. Construct Build Mater 2021;269:121310. https://doi.org/10.1016/j.conbuildmat.2020.121310.
[78] Land G, Stephan D. Controlling cement hydration with nanoparticles. Cement Concr Compos 2015;57:64–7.
[79] Singh L, Zhu W, Howind T, Sharma U. Quantification and characterization of CSH in silica nanoparticles incorporated cementitious system. Cement Concr Compos 2017;79:106–16.